



Bi-material microstructural design of chiral auxetic metamaterials using topology optimization

Huikai Zhang, Yangjun Luo, Zhan Kang*

State Key Laboratory of Structural Analysis for Industrial Equipment, Dalian University of Technology, Dalian 116024, China



ARTICLE INFO

Keywords:

Mechanical metamaterial
Chiral auxetic metamaterial
Bi-material microstructure
Topology optimization
Independent point-wise interpolation

ABSTRACT

This paper presents a new bi-material microstructural design method for chiral auxetic metamaterials. Based on the independent point-wise density interpolation (IPDI) and a bi-material model, optimal design problem of periodic unit cells is formulated using nodal density variables. The design objective is to minimize the Poisson's ratio while satisfying the specified volume constraints of the hard and soft materials, and the effective elastic properties of the bi-material microstructure are computed by the asymptotic homogenization method under periodic boundary conditions. This topology optimization problem is solved with a gradient-based mathematical programming algorithm on the basis of the sensitivity analysis. Several numerical examples, regarding design of anisotropic, orthogonal anisotropic and isotropic bi-material microstructures of chiral auxetic metamaterials, are given to demonstrate the effectiveness of the method. It is shown that the proposed bi-material design optimization method can be used to improve the performance of chiral auxetic metamaterials through enlarging the design space.

1. Introduction

Mechanical metamaterials with negative Poisson's ratios (NPRs) [1,2], also known as auxetic metamaterials [3], have attracted considerable interests. Such a material expands in the lateral direction when uniaxial stretch loads are applied and *vice versa*. Because of their special mechanical properties, auxetic metamaterials have potential applications in a wide range of fields, including medical and biomedical engineering [4], sport equipment and textile industries [2,5]. Moreover, auxetic materials may be useful to improve fracture toughness [6,7], acoustic energy absorption [8–11], and resistance to shear [12,13].

Although most conventional materials in nature possess positive Poisson's ratios, the classical theory of elasticity allows the Poisson's ratio of a material to be negative. Lakes [1,14] was the pioneer who designed the first artificial auxetic metamaterials. Since his work, many studies on auxetic metamaterials have been reported [2] and their application in various fields of research and engineering became an interesting topic. Novel multi-material 3D printing techniques have created new possibilities of fabricating NPR microstructures composed of two constituent materials [15]. In recent years, auxetic metamaterials with mechanical chirality, which can transform a linear deformation into rotation and twist deformations, have also been studied [16–19]. Additionally, the chirality concept has also been used to design optical

and thermal metamaterials [20–22]. Up to now, conventional meta-material design still relies to some extent on the designer's intuition, and thus limits the design space.

Topology optimization [23,24] recasts a structural design problem into a mathematical programming problem. To date, topology optimization has been widely applied in various engineering fields [25,26], including material design [27–29]. Among others, the solid isotropic material with penalty (SIMP) method [24], evolutionary structural optimization method [30], and level-set method [23] have achieved popularity. Since the microstructures are crucial to the effective properties of a metamaterial, many researchers have investigated the design of microstructures using topology optimization techniques. Sigmund [29] first introduced topology optimization into material design, and proposed an inverse homogenization approach to design a re-entrant structure with negative Poisson's ratios. Schwerdtfeger et al. [31] and Andreassen et al. [32] used topology optimization to design isotropic, re-entrant 3D microstructures with negative Poisson's ratios and verified their optimal results with experiments. Xia et al. [33] provided a simple MATLAB code for density-based topology optimization of NPR microstructures. Clausen et al. [34] further studied topology optimization of 3D NPR materials undergoing large-deformation. Ganghofer et al. [35] used topological derivative to design auxetic microstructures, where the mechanical properties were studied with the couple stress theory and experiments. Wang et al. [28] presented a level set method

* Corresponding author.

E-mail address: zhankang@dlut.edu.cn (Z. Kang).

for the design of isotropy and symmetric NPR materials. Recently, topological design of re-entrant NPR microstructures composed of multiple material phases has also been studied [36,37]. These studies have provided useful tools for the design of NPR materials with the re-entrant deformation mechanism.

Apart from the re-entrant configuration of microstructures, the chiral (or rotating) mechanism is another deformation mechanism realizing artificial NPR materials. Chiral microstructures are characterized by noncentrosymmetric configurations, which do not superimpose on their mirror images. In contrast to the re-entrant counterparts, a chiral metamaterial achieves the NPR effect mainly through the deformation of rotating ligaments. These ligaments easily rotate around the joints when external forces are applied. Additionally, under the periodic boundary condition, the chiral configuration allows interlocking of unit cells more easily to occur. Therefore, chiral auxetic metamaterials have a potential to be used as crash-resistant materials [7]. Due to their unique deformation characteristics, design of chiral auxetic materials has attracted considerable attention [15,16,38,39]. However, using topology optimization to design chiral mechanical metamaterials that exhibit NPR properties has not been systematically studied. This may be partly due to the difficulty of satisfying highly nonlinear design constraints (e.g. the orthogonal anisotropy and isotropy constraints of the effective material properties) when using some existing topology optimization formulations. Moreover, it is envisaged that the multi-material design concept can be used to improve the desired chiral property while still ensuring the required stiffness of the NPR materials. To this end, this paper focuses on the topological design of bi-material chiral auxetic microstructures. In the optimization models, three different metamaterial properties, namely, anisotropy, orthogonal anisotropy and isotropy are to be achieved. The twisting behavior of 3D periodic array structures assembled from the optimized chiral microstructures under axial loading is also studied using finite element simulations.

The remainder of this paper is organized as follows. In Section 2, we first introduce the independent point-wise density interpolation (iPDI) method, and present the basic concepts of the asymptotic homogenization. Then, Section 3 presents the topology optimization framework and the sensitivity analysis. In Section 4, several numerical examples for achieving anisotropic, orthogonal anisotropic and isotropic NPR properties are given. The advantages of the bi-material chiral auxetic metamaterials in comparison to single-material ones are demonstrated. Finite element simulations of periodic array structures composed of the optimized microstructural unit cells are also performed. Conclusions are given in Section 5.

2. Material interpolation model and effective property analysis of unit cells

We adopt the iPDI method [40] to construct a point-wise density field representing the material distribution in the considered topology optimization of bi-material microstructural unit cells, and establish the relation between the Young's modulus of materials and nodal densities using the multi-material SIMP method. Then the asymptotic homogenization method for evaluating the effective material properties of the metamaterial unit cells is briefly introduced.

2.1. Independent point-wise density interpolation model

In the iPDI method, the density field is constructed with interpolation of density values at the design variable points, also referred to as density points (plotted as green points in Fig. 1). Our previous study showed that the iPDI method was able to improve the boundary description quality in topology optimization [41]. In this study, we use the eight-node quadratic quadrilateral (Q8) elements [40] to discrete the unit cell, and the density points are positioned at the finite element nodes for simplicity of implementation. Using these high-order

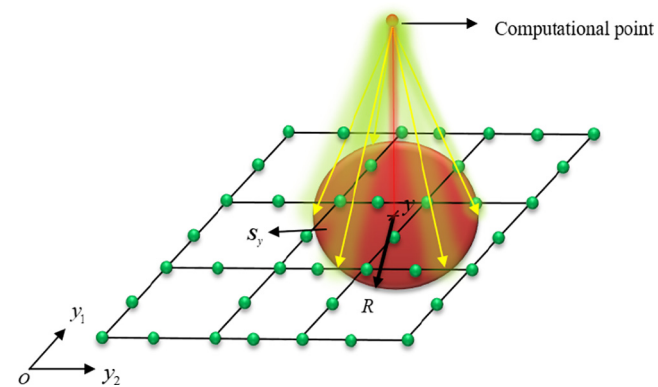


Fig. 1. Design variables within a specified influence domain are used to interpolate the material density field at point y .

elements helps to avoid the 'islanding' phenomenon [42].

For a single-material topology optimization problem, the iPDI model is expressed by

$$\rho(y) = \sum_{i \in S_y} \omega_i(y) x_i \quad (1)$$

Here, $\rho(y)$ is the density field representing the material distribution in the design domain, x_i is the relative density of the i th density point, S_y is a specified influence domain (here, a circular domain with a cutoff radius R , as shown in Fig. 1), and ω_i is a weight coefficient with the following form

$$\omega_i(y) = D_i(y) / \sum_{j \in S_y} D_j(y), \quad D_i(y) = 1/d_i^2 \quad (2)$$

where $d_i(y) = \|y - y_i\|_2$ is the Euclidean distance between the computational point y and the density point y_i .

The iPDI interpolation model has a range-restricted property, that is

$$\min_{i \in S_y} \{x_i\} \leq \rho(y) \leq \max_{i \in S_y} \{x_i\} \quad (3)$$

The range-restricted property of the iPDI model is necessary for a material density interpolation in topology optimization to ensure its physical meaning [40]. Recently, this model has also been extended to the ply orientation design of fiber-reinforced composite structures [43,44].

2.2. Multi-material interpolation

In this study, we consider three material phases for the microstructure design: hard material, soft material and voids [45]. The multi-material SIMP interpolation, in conjunction with the iPDI model, is employed:

$$E(y) = \rho_1(y)^{p_1} (\rho_2(y)^{p_2} E_H + (1 - \rho_2(y)^{p_2}) E_S) \quad (4)$$

where

$$\rho_1(y) = \sum_{i \in S_y} \omega_i(y) x_1^i, \quad \rho_2(y) = \sum_{i \in S_y} \omega_i(y) x_2^i \quad (5)$$

In Eq. (4), E , E_H and E_S are respectively the elastic moduli of the mixture, the hard material and the soft material; x_1^i and x_2^i are the relative material densities of the density points. The quantities p_1 , p_2 ($p_1, p_2 \geq 3$) are penalty factors. The density field $\rho_1(y) = 1$ indicates presence of the materials at position y ; while $\rho_1(y) = 1$ and $\rho_2(y) = 1$ stands for the hard material, and $\rho_1(y) = 1$ and $\rho_2(y) = 0$ stands for the soft material. Specifically, the elastic modulus satisfies the following relations

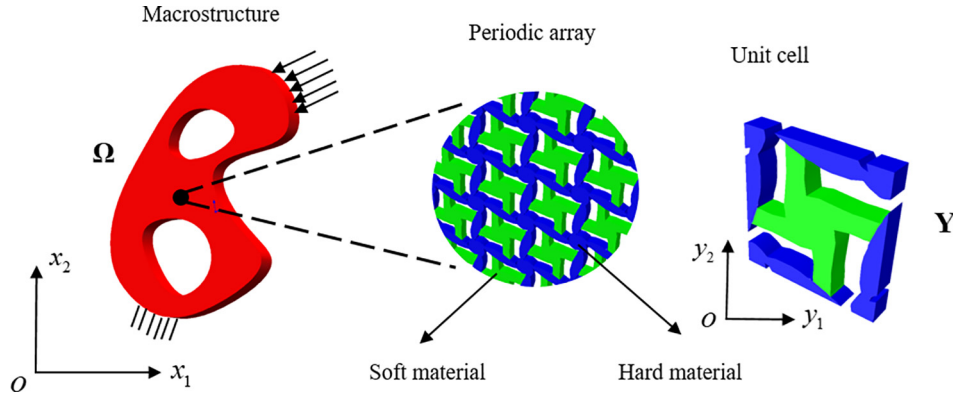


Fig. 2. Macroscopic structure, microscopic array structure and periodic unit cell.

$$E(y) = \begin{cases} 0 & \rho_1(y) = 0 \\ E_H & \rho_1(y) = 1, \rho_2(y) = 1 \\ E_S & \rho_1(y) = 1, \rho_2(y) = 0 \end{cases} \quad (6)$$

The material volumes can be written as

$$\begin{aligned} V_T &= \int_Y \rho_1(y) dy \\ V_H &= \int_Y \rho_1(y) \rho_2(y) dy \\ V_S &= \int_Y \rho_1(y)(1-\rho_2(y)) dy \end{aligned} \quad (7)$$

where V_T is the total material volume, V_H and V_S are respectively the volumes of the hard material and soft material, Y denotes the whole design domain for the microstructure.

2.3. Asymptotic homogenization of unit cells

The asymptotic homogenization method [29] is based on rigorous mathematical theories, and is used to predict the effective properties of periodic microstructures in the considered metamaterial design problem, as shown in Fig. 2.

In the asymptotic homogenization method, the macroscopic displacement field is expressed using a small-parameter perturbation

$$u_\xi(\mathbf{x}, \mathbf{y}) = u_0(\mathbf{x}, \mathbf{y}) + \xi^1 u_1(\mathbf{x}, \mathbf{y}) + \xi^2 u_2(\mathbf{x}, \mathbf{y}) + \dots \quad (8)$$

where \mathbf{x} and \mathbf{y} are the vectors of the macroscopic and microscopic coordinates, $\xi \rightarrow 0$ is an infinitesimal positive number and it relates the macro scale and the micro scale with $\mathbf{y} = \mathbf{x}/\xi$, $u_0(\mathbf{x}, \mathbf{y})$, $u_i(\mathbf{x}, \mathbf{y})$, ... are Y -periodic smooth displacement perturbation functions (Y is the side length of the unit cell).

Considering only the first-order terms in the asymptotic expansion in (8), the effective elasticity of the unit cell can be written in the energy form as

$$\mathbf{D}^H = \frac{1}{|Y|} \int_Y C_{pqrs} (\epsilon_{pq}^{0(ij)} - \epsilon_{pq}^*(\chi^{ij})) (\epsilon_{rs}^{0(kl)} - \epsilon_{rs}^*(\chi^{kl})) dy \quad (i,j,k,l = 1,2,\dots,d) \quad (9)$$

where d is the spatial dimension ($d = 2$ for the considered two-dimensional problem), Y and $|Y|$ are respectively the domain and volume of the periodic unit cell. The isotropic constitutive matrix has the form $\mathbf{C} = EC_0$, with \mathbf{C}_0 being the non-dimensional constitutive matrix:

$$\mathbf{C}_0 = \frac{1}{1-\nu^2} \begin{bmatrix} 1 & \nu & 0 \\ \nu & 1 & 0 \\ 0 & 0 & (1-\nu)/2 \end{bmatrix} \quad (10)$$

Here, ν is Poisson's ratio.

In Eq. (9), the characteristic displacement field $\chi \in \widetilde{V}_\psi$ of the unit cell is the solution to the following micro-scale problem [29]:

$$\int_Y C_{pqrs} \epsilon_{pq}(v^{ij}) \epsilon_{rs}^*(\chi^{kl}) dy = \int_Y C_{pqrs} \epsilon_{pq}(v^{ij}) \epsilon_{rs}^0(\chi^{kl}) dy, \quad \forall v \in \widetilde{V}_\psi \quad (11)$$

where v is the virtual displacement, and $\widetilde{V}_\psi = \{v: v \text{ is } Y\text{-periodic}\}$ is the space of virtual displacements. The fluctuation strain $\epsilon_{rs}^*(\chi^{kl})$ is defined through the strain-displacement relations $\epsilon_{rs}^*(\chi^{kl}) = (\partial\chi_r^{kl}/\partial y_s + \partial\chi_s^{kl}/\partial y_r)/2$, and $\epsilon_{rs}^{0(kl)}$ represents the three independent unit test strain fields, namely the horizontal unit strain $\epsilon_{rs}^{0(11)} = (1,0,0)^T$, the vertical strain $\epsilon_{rs}^{0(22)} = (0,1,0)^T$ and the shear unit strain $\epsilon_{rs}^{0(12)} = (0,0,1)^T$.

3. Formulation of topology optimization and sensitivity analysis

3.1. Mathematical statement of topology optimization

Topology optimization of multi-material chiral auxetic metamaterials can be formulated as

$$\begin{aligned} &\text{Find } \mathbf{x}_1, \mathbf{x}_2 \\ &\text{to minimize } f(\mathbf{D}^H) \\ &\text{subject to } \int_Y C_{pqrs} \epsilon_{pq}(v^{ij}) \epsilon_{rs}^*(\chi^{kl}) dy = \int_Y C_{pqrs} \epsilon_{pq}(v^{ij}) \epsilon_{rs}^{0(kl)} dy \quad \forall v \in \widetilde{V}_\psi \\ &V_T \leq f_T V_0 \\ &V_H \leq f_H V_0 \\ &g(\mathbf{D}^H) = 0 \\ &0 < x_{\min} < x_1^i \leq 1, 0 \leq x_2^i \leq 1 (i = 1, 2, \dots, N) \end{aligned} \quad (12)$$

where $\{\mathbf{x}_1^1, \mathbf{x}_1^2, \dots, \mathbf{x}_1^N\}^T$, $\{\mathbf{x}_2^1, \mathbf{x}_2^2, \dots, \mathbf{x}_2^N\}^T$ are the vectors of design variables; f_T , f_H , and f_S are the volume fractions of the total material, the hard material and the soft material, respectively; V_0 is the whole volume of the unit cell, and N is the total number of density points.

The effective elasticity tensors can be written in the following matrix form

$$\mathbf{D}^H = \begin{bmatrix} D_{1111} & D_{1122} & D_{1166} \\ & D_{2222} & D_{2266} \\ \text{Sym} & & D_{6666} \end{bmatrix} \quad (13)$$

The optimization objective in (12) is defined as the function of the effective elasticity constants of the microstructure [33]

$$f(\mathbf{D}^H) = D_{1122} - q^n (D_{1111} + D_{2222}) \quad q \in (0, 1) \quad (14)$$

where n is the iteration number of the topology optimization process, q is a prescribed constant, which is set to be 0.8 in this study. It is obvious that the objective function approaches D_{1122} with increasing n . The component D_{1122} is negative for anisotropic NPs metamaterials, therefore we expect to obtain a microstructure exhibiting a chiral negative Poisson's ratio through minimizing this objective function from an initial chirality configuration to achieve a negative value of D_{1122} .

However, the resulting chirality NPs metamaterials obtained by

minimizing the mentioned objective function may be anisotropic. Therefore, we include a material symmetry constraint $g(\mathbf{D}^H) = 0$ in the optimization problem (12) to impose orthogonal anisotropic or isotropic constraints. This constraint function is defined as [46,47]

$$g = \begin{cases} \frac{D_{1166}^2 + D_{2266}^2}{(D_{1111} + D_{2222})^2} & \text{Orthogonal anisotropy} \\ \frac{((D_{1111} + D_{2222}) - 2(D_{1122} + 2D_{6666}))^2 + (D_{1111} - D_{2222})^2}{(D_{1111} + D_{2222})^2} & \text{Isotropy} \end{cases} \quad (15)$$

In Eq. (13), all the components are nonzero ones for anisotropic chirality NPRs. The orthogonal anisotropic constraint in Eq. (15) requires that the components D_{1166} , D_{6611} , D_{2266} and D_{6622} are all zeros. Further, the isotropic constraint imposes the relations $D_{1111} = 2D_{6666} + D_{1122}$ and $D_{1111} = D_{2222}$.

The equilibrium equation for determine the characteristic displacement χ in Eq. (11) has the following discrete form in the finite element analysis

$$\mathbf{K}\chi = \mathbf{F} \quad (16)$$

where \mathbf{K} and \mathbf{F} are the global stiffness matrix and the load vector of the unit cell, respectively. They are given by

$$\mathbf{K} = \sum_{e=1}^M \mathbf{k}^e = \sum_{e=1}^M \int_{\Omega_e} \mathbf{B}^T \mathbf{C} \mathbf{B} dy_e, \quad \mathbf{F} = \sum_{e=1}^M \mathbf{f}^e = \sum_{e=1}^M \int_{\Omega_e} \mathbf{B}^T \mathbf{C} \mathbf{e}^0 dy_e \quad (17)$$

where \mathbf{k}^e and \mathbf{f}^e are respectively the stiffness matrix and the load vector of element e , M is the number of finite elements in the unit cell, and \mathbf{B} is the strain-displacement matrix.

3.2. Sensitivity analysis

The sensitivity analysis of the objective function, constraint functions are presented in this section. The derivatives of the objective function with respect to the design variables are expressed as:

$$\frac{\partial f(\mathbf{D}^H)}{\partial x_m^i} = \frac{\partial f(\mathbf{D}^H)}{\partial \mathbf{D}^H} \frac{\partial \mathbf{D}^H}{\partial x_m^i} \quad (i = 1, 2, \dots, N; m = 1, 2) \quad (18)$$

where $m = 1$ and $m = 2$ represent the hard material and soft material, respectively. The sensitivity of the effective elastic matrix has the following form

$$\begin{aligned} \frac{\partial \mathbf{D}^H}{\partial x_m^i} &= \frac{1}{|\mathbf{Y}|} \frac{\partial \int_{\mathbf{Y}} C_{pqrs} (\varepsilon_{pq}^{0(ij)} - \varepsilon_{pq}^{*(ij)}) (\varepsilon_{rs}^{0(kl)} - \varepsilon_{rs}^{*(kl)}) dy}{\partial x_m^i} \\ &= \frac{1}{|\mathbf{Y}|} \int_{\mathbf{Y}} \frac{\partial C_{pqrs}}{\partial x_m^i} (\varepsilon_{pq}^{0(ij)} - \varepsilon_{pq}^{*(ij)}) (\varepsilon_{rs}^{0(kl)} - \varepsilon_{rs}^{*(kl)}) dy \\ &\quad - \frac{2}{|\mathbf{Y}|} \int_{\mathbf{Y}} C_{pqrs} \frac{\partial \varepsilon_{pq}^{*(ij)}}{\partial x_m^i} (\varepsilon_{rs}^{0(kl)} - \varepsilon_{rs}^{*(kl)}) dy \\ &= \frac{1}{|\mathbf{Y}|} \int_{\mathbf{Y}} \frac{\partial C_{pqrs}}{\partial x_m^i} (\varepsilon_{pq}^{0(ij)} - \varepsilon_{pq}^{*(ij)}) (\varepsilon_{rs}^{0(kl)} - \varepsilon_{rs}^{*(kl)}) dy - \dots \\ &\quad - \frac{2}{|\mathbf{Y}|} \left(\int_{\mathbf{Y}} C_{pqrs} \frac{\partial}{\partial y_q} \left(\frac{\partial \chi_p^{*(ij)}}{\partial x_m^i} \right) \varepsilon_{rs}^{0(kl)} dy - \int_{\mathbf{Y}} C_{pqrs} \frac{\partial}{\partial y_q} \left(\frac{\partial \chi_p^{*(ij)}}{\partial x_m^i} \right) \varepsilon_{rs}^{*(kl)} dy \right) \end{aligned} \quad (19)$$

Note that Eq. (11) has another form

$$\int_{\mathbf{Y}} C_{pqrs} \frac{\partial}{\partial y_q} (\mathbf{v}_p^{ij}) \varepsilon_{rs} (\chi^{*kl}) dy - \int_{\mathbf{Y}} C_{pqrs} \varepsilon_{pq}^{0(ij)} \frac{\partial \mathbf{v}_r^{kl}}{\partial y_s} dy = 0, \quad \forall \mathbf{v} \in \widetilde{\mathbf{V}}_\psi \quad (20)$$

In the last term of Eq. (19), the derivatives of the characteristic displacement field with respect to the design variables $\partial \chi_p^{*(ij)} / \partial x_m^i$ belong to the same periodic space $\widetilde{\mathbf{V}}_\psi$ as the characteristic displacement

fields χ . Therefore, the virtual displacement \mathbf{v} in Eq. (20) can be replaced by $\partial \chi_p^{*(ij)} / \partial x_m^i$, which leads to

$$\int_{\mathbf{Y}} C_{pqrs} \frac{\partial}{\partial y_q} \left(\frac{\partial \chi_p^{ij}}{\partial x_m^i} \right) \varepsilon_{rs} (\chi^{*kl}) dy - \int_{\mathbf{Y}} C_{pqrs} \varepsilon_{pq}^{0(ij)} \frac{\partial}{\partial y_s} \left(\frac{\partial \chi_r^{*kl}}{\partial x_m^i} \right) dy = 0 \quad (21)$$

Inserting Eq. (21) into Eq. (19), we obtain the sensitivity of the effective elastic matrix with respect to the design variables as

$$\frac{\partial \mathbf{D}^H}{\partial x_m^i} = \frac{1}{|\mathbf{Y}|} \int_{\mathbf{Y}} \frac{\partial C_{pqrs}}{\partial x_m^i} (\varepsilon_{pq}^{0(ij)} - \varepsilon_{pq}^{*(ij)}) (\varepsilon_{rs}^{0(kl)} - \varepsilon_{rs}^{*(kl)}) dy \quad (22)$$

Here, the derivations of the constitutive matrix \mathbf{C} with respect to design variables can be deduced using the interpolation model in Eq. (4).

$$\frac{\partial \mathbf{C}}{\partial x_1^i} = p_1 \rho_1(y)^{(p_1-1)} \omega_i(y) (\rho_2(y) E_H + (1-\rho_2(y)) E_S) \mathbf{C}_0$$

$$\frac{\partial \mathbf{C}}{\partial x_2^i} = p_2 \rho_1(y) \rho_2(y)^{(p_2-1)} \omega_i(y) (E_H - E_S) \mathbf{C}_0 \quad (23)$$

where

$$\frac{\partial \rho_{1,2}(y)}{\partial x_m^i} = \begin{cases} \omega_i(y) & i \in S_y \\ 0 & i \notin S_y \end{cases} \quad (m = 1, 2) \quad (24)$$

In addition, the sensitivities of volume constraints have the following forms

$$\begin{cases} \frac{\partial V_T}{\partial x_1^i} = \int_{\mathbf{Y}} \omega_i(y) dy & \frac{\partial V_T}{\partial x_2^i} = 0 \\ \frac{\partial V_H}{\partial x_1^i} = \int_{\mathbf{Y}} \omega_i(y) \rho_2(y) dy & \frac{\partial V_H}{\partial x_2^i} = \int_{\mathbf{Y}} \rho_1(y) \omega_i(y) dy \quad \forall i \in S_y \\ \frac{\partial V_S}{\partial x_1^i} = \int_{\mathbf{Y}} \omega_i(y) (1-\rho_2(y)) dy & \frac{\partial V_S}{\partial x_2^i} = - \int_{\mathbf{Y}} \rho_1(y) \omega_i(y) dy \end{cases} \quad (25)$$

3.3. Numerical implementation

The flowchart of the proposed method is given in Fig. 3. First, the initial values of the design variables x_1 and x_2 are given. Then, the Young's moduli of the constituent materials in the unit cell are interpolated with the IPDI model given in Eq. (4). The finite element analysis with periodic boundary conditions is then performed on the unit cell, and the effective material properties, the objective function, the constraints and the corresponding sensitivities are obtained. Finally, the method of moving asymptotes (MMA) optimizer [48] is used to update the density design variables. This process is repeated until the prescribed stopping criterion is met.

4. Numerical examples

In this section, we first carry out microstructural topology optimization of anisotropic, orthogonal anisotropic and isotropic chiral auxetic metamaterials using the proposed method. Then, we compare the effective material properties of the orthogonal and isotropic chiral auxetic metamaterials. Finally, we perform linear finite element analysis of the periodic array structures composed of the optimized unit cells using the software ABAQUS.

In the numerical examples, the effective Poisson's ratios, effective bulk and shear moduli of the optimized chiral NPRs metamaterials are evaluated. The effective Poisson's ratio of isotropic chirality NPR metamaterials is given by $\mu = D_{1122}/D_{1111} = D_{2211}/D_{2222}$. For the orthogonal anisotropic chirality NPR metamaterial, we compute the effective Poisson's ratios μ_{12} and μ_{21} in the two principal directions using the components of the effective compliance matrix as [49] $\mu_{12} = -S_{12}/S_{22}, \mu_{21} = -S_{21}/S_{11}$. Because there are no definitions of real

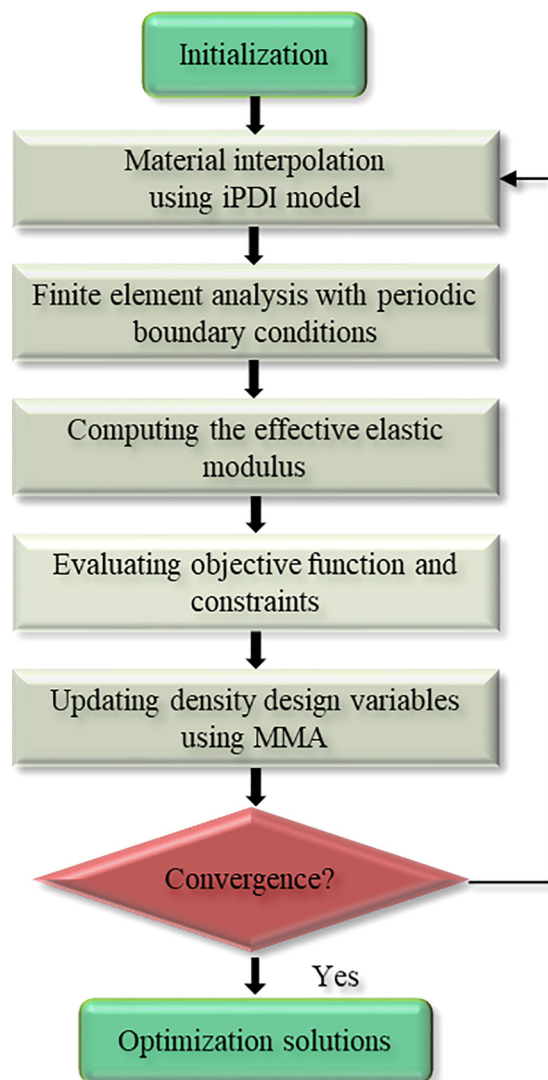


Fig. 3. Flowchart of the proposed method.

Poisson's ratio for the anisotropic chirality NPRs, we consider the ratios $\mu_{12}^* = D_{1122}/D_{1111}$ and $\mu_{21}^* = D_{1122}/D_{2222}$ as an approximate measure of deformation ratio in the two principal directions for the case of anisotropic chiral NPRs metamaterials, and refer to them as quasi-effective Poisson's ratios. The bulk modulus K for the isotropic NPR metamaterials, and the quasi-effective bulk modulus K^* for the anisotropic and orthogonal anisotropic chiral NPR metamaterials are computed as $(D_{1111} + D_{2222} + D_{1122} + D_{2211})/4$. The effective shear moduli for all the cases are evaluated as $G = D_{6666}$.

For all the examples considered in this section, the Poisson's ratios are $\nu_H = \nu_S = 0.3$, and the Young's moduli for the hard (E_H) and (E_S) soft materials are respectively 10 Gpa and 2 Gpa. Square plane stress elements with unit size are used in the finite element discretization.

In order to obtain optimized microstructures with desired chirality, we introduce chiral initial configurations as schematically shown in Fig. 4, and set the initial design variable values to $x_1^i = x_2^i = f_T$ ($i = 1, 2, \dots, N$). As examples, the effective properties of such initial designs with the total volume fraction $f_T = 0.6$ are listed in Table 1.

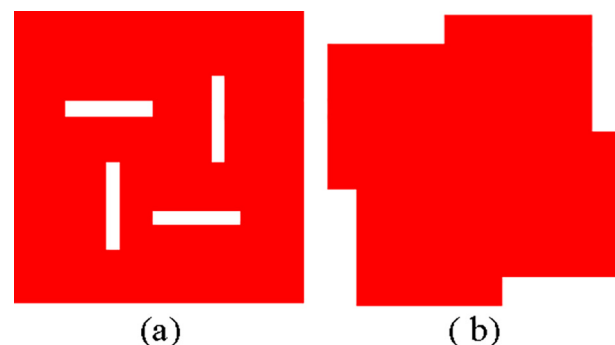


Fig. 4. Initial designs for topology optimization of unit cells. The red color indicates presence of materials (with the same initial volume ratios for hard and soft materials), and the white color represents voids. (a) Initial design adopted in Sections 4.1 and 4.2, (b) initial design adopted in Section 4.3. (For interpretation of the references to color in this figure legend, the reader is referred to the web version of this article.)

4.1. Topology optimization of anisotropic chiral auxetic metamaterials

4.1.1. Single-material and bi-material microstructures for chiral auxetic metamaterials

We now consider topology optimization of bi-material anisotropic microstructures for chiral auxetic metamaterials. The volume fractions of the hard material and soft material are 20% and 30%, respectively. For comparison, the optimized single-material designs are also given, in which the soft material is used and the material volume fraction is 50%. The design domain is discretized with 71×71 elements, and the cutoff radius R in the iPDI model is 1.5. We adopt the initial configuration shown in Fig. 4(a).

The optimization solutions for the single-material and bi-material microstructures are shown in Fig. 5(a) and (c), respectively. Fig. 5(b) and (d) are the 4×4 arrays of the optimized unit cells. The black and gray colors represent the hard and soft materials, respectively. It is seen that the final designs have clear and smooth boundaries. In Fig. 5(c), the hard material forms the major frame and joints of the unit cell, while the soft material locates at connection regions and the central area, and provides certain flexibility to enhance the NPR effect. Note that the tensile-shear coupling terms D_{1166} , D_{6611} , D_{6622} , and D_{2266} are nonzero under the anisotropic conditions.

The optimized quasi-effective Poisson's ratios for the single-material design (Fig. 5(a)) are $\mu_{12}^* = \mu_{21}^* = -0.713$, while the values for the bi-material design (Fig. 5(b)) are $\mu_{12}^* = \mu_{21}^* = -0.806$. This shows that the optimized bi-material microstructural unit cell has a larger NPR effect as compared with the single-material one.

The value of quasi-effective bulk modulus K^* is 43.700 Mpa for the bi-material auxetic microstructure, which is higher than the value 29.375 Mpa for the single-material design. Also, the bi-material design has a higher shear modulus G (22.849 Mpa v.s. 13.077 Mpa). This shows that the bi-material NPR microstructural design is able to achieve a larger overall stiffness as compared with single-material design.

Fig. 6(a) depicts the iteration histories of the quasi-effective Poisson's ratio μ_{12}^* and the objective function f , and Fig. 6(b) shows the corresponding iteration histories of the total material volume fraction f_T and the hard-material volume fraction f_H for the bi-material design in Fig. 5(c). Some selected intermediate designs are shown in Fig. 6(c). As can be seen from the figures, the topology optimization iteration converges very fast. In this example, although we let the topology optimization iteration to run for 250 steps, and main features of the load transmission path of the unit cell have been formed within the first

Table 1
Effective elastic matrices and effective properties of initial designs ($f_T = 0.6$).

Microstructure shown in Fig. 4(a)	Microstructure shown in Fig. 4(b)
$D^H = \begin{bmatrix} 362.901 & 108.447 & -0.136 \\ 108.447 & 362.901 & 0.136 \\ -0.136 & 0.136 & 126.772 \end{bmatrix}$ (Mpa) $\mu_{12}^* = \mu_{21}^* = 0.299$ $K^* = 235.674$ Mpa $G = 126.772$ Mpa	$D^H = \begin{bmatrix} 334.823 & 99.139 & 0.5301 \\ 99.139 & 334.8234 & -0.5301 \\ 0.5301 & -0.5301 & 117.1475 \end{bmatrix}$ (Mpa) $\mu_{12}^* = \mu_{21}^* = 0.296$ $K^* = 216.981$ Mpa $G = 117.148$ Mpa

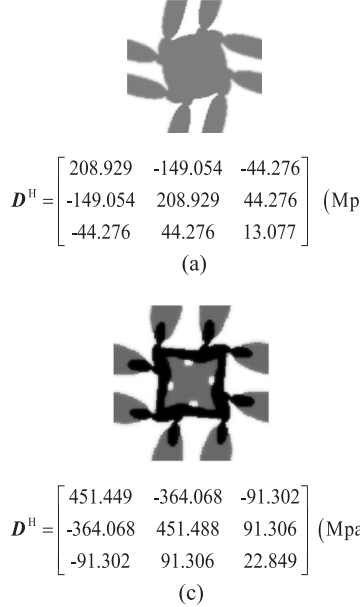


Fig. 5. Optimization solutions of the anisotropic microstructures for chiral auxetic metamaterials. (a) Single-material design; (b) 4 × 4 array of the single-material unit cell; (c) bi-material design; (d) 4 × 4 array of the bi-material unit cell.

thirty steps, and after that the material boundaries change only slightly in local areas. This demonstrates the validity of the proposed method.

The optimized load paths for both bi-material and single-material microstructures are similar, and they closely resemble the classical chiral Ligament structures [38,39]. The deformation mechanism of the optimized bi-material chiral microstructure is illustrated in Fig. 7, in which the colored regions indicate the periodic boundary conditions. This unit cell has three main parts: the ligaments, the joints, and the central part. The microstructure undergoes a clockwise rotation under application of bi-axial loading conditions. The rotating deformation arises from the ligament deformation around the joints. This mechanism of deformation differs greatly from that of a re-entrant microstructure.

4.1.2. Effects of hard material volume fractions

We now study the influences of the material volume fractions f_H (hard material) and f_S (soft material). To this end, we fix the total material volume ratio at $f_T = 60\%$, and run the topology optimization process for different combinations listed in Table 2. Table 3 presents the optimization results. Again, for the bi-material designs (Cases 2, 3, and 4), the hard material acts as the joints and main load-bearing members, whereas the soft material is mainly located at the connection regions or attached to the hard material members. Such a pattern helps to enhance

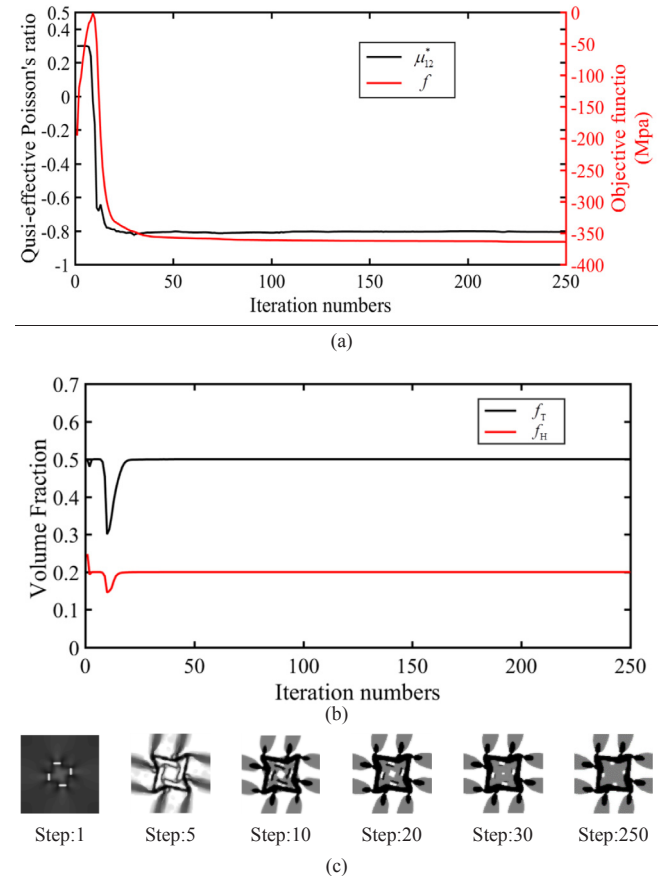


Fig. 6. Iteration histories of the topology optimization of bi-material chiral auxetic microstructure. (a) Quasi-effective Poisson's ratio μ_{12}^* and objective function f ; (b) volume ratios f_T and f_H ; (c) selected intermediate designs.

the NPR effects while still retaining the stiffness of the microstructure, as revealed by comparison between the bi-material and single-material designs.

It is also seen from Fig. 8 that the quasi-effective bulk modulus and shear modulus increase with f_H . However, this is not the case for the quasi-effective Poisson's ratios μ_{12}^* and μ_{21}^* , which implies that a compromise should be made when choosing an appropriate volume-fraction combination of the hard and soft materials to achieve a desired NPR property.

Fig. 8(b) shows that the plane shear modulus G is smaller than the quasi-effective bulk modulus K^* for all the cases, even when the values of μ_{12}^* and μ_{21}^* are both smaller than -0.5 . This indicates that the optimized anisotropic auxetic microstructures have a relatively low ability to resist shear deformation in comparison to conventional isotropic

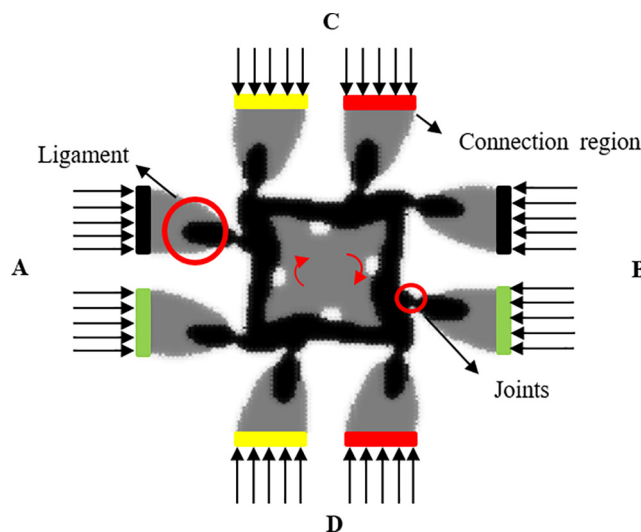


Fig. 7. Rotating deformation mechanism of the optimized chiral auxetic metamaterial.

Table 2

Different cases of material volume fractions f_H (hard material) and f_S (soft material).

Case	f_H	f_S
1	0%	60%
2	15%	45%
3	30%	30%
4	45%	15%
5	60%	0%

auxetic materials.

4.2. Topology optimization of orthogonal anisotropic bi-material chiral auxetic metamaterials

In this section, we optimize the microstructures under the orthogonality constraint expressed by Eq. (15). The value of f_T and f_H are 60% and 45%, respectively. The number of finite element mesh is 60×60 , and the cut-off radius is $R = 2$. The obtained optimization results are given in Fig. 9. The optimized load path has remarkable differences compared with classical chiral ligament structure [2].

In this design, the coupling components D_{1166} , D_{6611} , D_{2266} and D_{6622} of the effective elastic modulus matrix become very small as a result of the orthogonality constraints. The constitutive law of the unit cell can be written as

$$\bar{\sigma} = D^H \bar{\varepsilon} \quad \text{or} \quad \bar{\varepsilon} = S^H \bar{\sigma} \quad (26)$$

where $\bar{\sigma}$ and $\bar{\varepsilon}$ are the average stress and strain of the periodic microstructure, and S^H is the effective compliance matrix, which is the inverse of the effective elastic matrix in equation (13), which can be written as [49]

$$S^H = (D^H)^{-1} = \begin{bmatrix} S_{11} & S_{12} & 0 \\ S_{12} & S_{22} & 0 \\ 0 & 0 & S_{66} \end{bmatrix} \quad (27)$$

where

$$S_{11} = \frac{1}{E_1}, S_{22} = \frac{1}{E_2}, S_{12} = \frac{-\mu_{12}}{E_2} = \frac{-\mu_{21}}{E_1}, S_{66} = \frac{1}{G_{12}} \quad (28)$$

The parameters E_1, E_2 and G_{12} are the principal direction elastic moduli and the plane shear modulus, respectively. The Poisson's ratios are $\mu_{12} = -0.720$ and $\mu_{21} = -0.720$. The quasi-effective bulk modulus K^* and shear modulus G are 117.843 Mpa and 151.997 Mpa.

4.2.1. Effects of hard material volume fractions

We now compare the optimization results for different volume fraction ratios of hard/soft materials as listed in Table 2. These results are summarized in Table 4. With increasing f_H (from Case 1 to Case 5), most of the hard material members tend to become stronger, though some thin members appear in Case 3 and Case 4. Our numerical experiences show that these thin bars will disappear when an increased cut-off radius R is used in the density interpolation. We also find that the periodic arrays for Case 1 and Case 5 are very similar to the Kirigami structures [50,51] that have been used in many fields.

Fig. 10(a) shows the changes of the Poisson's ratios μ_{12} and μ_{21} versus the hard material fraction f_H . Both Poisson's ratios attain their minimum values for the case $f_H = 45\%$. There is a strong oscillation in Fig. 10(a). This may be due to the large topological changes for different usage of the hard material. Moreover, the quasi-effective bulk modulus K^* and the shear modulus G increase monotonically with increasing f_H in Fig. 10(b). For all the cases of material fraction values, the shear moduli obtained under the orthogonal constraint are higher than those under the anisotropy constraint, as can be seen from Fig. 8(b) and Fig. 10(b). Also, in contrast to the case of anisotropic design, the quasi-effective bulk modulus K^* and the shear modulus G have very close values in the orthogonal anisotropic design.

4.2.2. Effects of total material volume fractions

In this example, we consider different total material volume fraction f_T ranging from 30% to 70% while keeping the ratios for the hard and soft f_H/f_S as 2/3. The values of f_T , f_H and f_S for the considered cases are listed in Table 5.

The optimization results for these cases are given in Table 6 and Fig. 11. The effective Poisson's ratio μ_{12} achieves its minimum value at $f_T = 50\%$. It is interesting to note that the shear modulus G becomes larger than the quasi-bulk modulus K^* for the case $f_T = 60\%$.

4.3. Comparisons between optimized orthogonal anisotropic and isotropic bi-material microstructures of chiral auxetic metamaterials

In this section, we compare the optimization results obtained under the orthogonal anisotropic and isotropic constraints. The initial material layout is shown in Fig. 4(b) and the cut-off radius is $R = 2.5$. The hard and soft materials volume fractions are respectively 30% and 30%.

When comparing the optimization results presented in Table 7, we find that the optimized isotropic microstructure has a relatively high shear modulus, and the orthogonal microstructure exhibits a balance between the quasi-effective bulk modulus and shear modulus. This shows that the stiffness of bi-material chiral microstructures can be tailored when achieving the negative Poisson's ratio through topology optimization.

4.4. Finite element verification of optimized metamaterials

We now perform the finite element simulations to verify the optimized metamaterial microstructures. We reconstruct the unit cell model

Table 3

Optimization results for different volume fractions under anisotropic condition.

Case	Unit cell	Array (4×4)	D^H (Mpa)	$\mu_{12}^*, \mu_{21}^*, K^*, G$ (Mpa)
1			$\begin{bmatrix} 178.787 & -118.854 & -39.154 \\ -118.154 & 178.788 & 39.154 \\ -39.154 & 39.154 & 12.866 \end{bmatrix}$	$-0.645, -0.6445$ $9.967, 12.866$
2			$\begin{bmatrix} 474.502 & -305.490 & -34.916 \\ -305.490 & 383.801 & 27.204 \\ -34.916 & 27.204 & 28.861 \end{bmatrix}$	$-0.644, -0.796$ $61.832, 28.861$
3			$\begin{bmatrix} 705.263 & -551.388 & 138.070 \\ -551.388 & 728.314 & -140.321 \\ 138.070 & -140.321 & 35.017 \end{bmatrix}$	$-0.782, -0.778$ $82.702, 35.017$
4			$\begin{bmatrix} 668.814 & -436.326 & -139.691 \\ -436.326 & 668.814 & 139.691 \\ -139.691 & 139.693 & 45.214 \end{bmatrix}$	$-0.652, -0.6521$ $16.244, 45.214$
5			$\begin{bmatrix} 878.713 & -579.363 & -200.202 \\ -579.363 & 878.713 & 200.202 \\ -200.20 & 200.202 & 69.092 \end{bmatrix}$	$-0.656, -0.656$ $149.678, 69.092$

($18.4 \times 18.4 \times 1$ mm) for the isotropy microstructure in Section 4.3, as shown in Fig. 12(a). The corresponding 8×16 periodic array structure, which is discretized using quadratic tetrahedron solid elements, is shown in Fig. 12(b).

To validate the negative Poisson's ratio effects, we apply a displacement of $\Delta V = 60$ mm (corresponding to a strain of 20.380%) to the 8×16 periodic array, while restricting the displacements in y and z directions at the bottom edge, and the displacement in x direction at the

black point marked in Fig. 13(b). The numerical results for the compressive and tensile loading conditions are shown respectively in Fig. 13(a) and (c). The Poisson's ratio is estimated as $\mu_{12} = -\Delta \bar{U} l_y / \Delta V l_x$. Here, $\Delta \bar{U}$ is average relative displacements of the red points marked in Fig. 13(b), l_x and l_y are the lengths of the periodic array structure in x and y directions. The Poisson's ratio μ_{12} predicted by this linear finite element model for the compressive and tensile conditions are both -0.672 , which has a 5.750% difference with the value of the

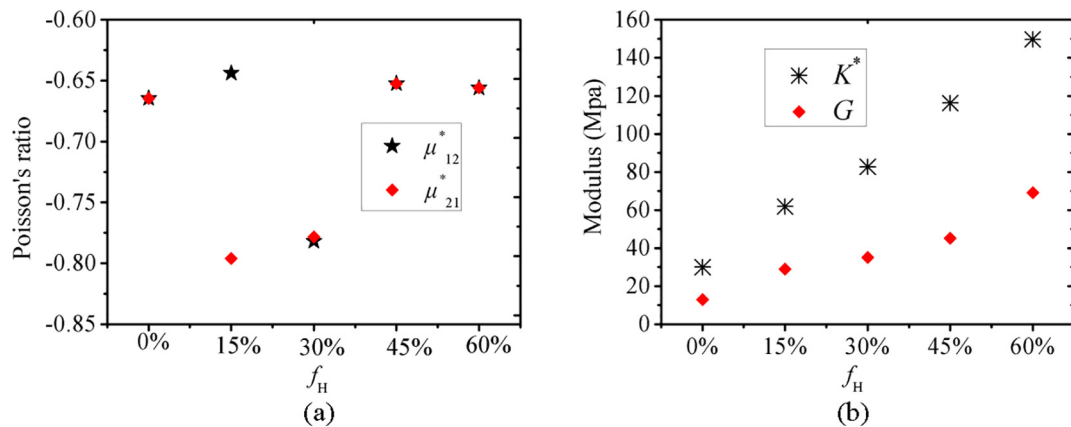


Fig. 8. Properties of the optimized designs obtained with different volume fractions of the hard material. (a) Quasi-effective Poisson's ratios μ_{12}^* and μ_{21}^* ; (b) quasi-effective bulk modulus K^* and shear modulus G .

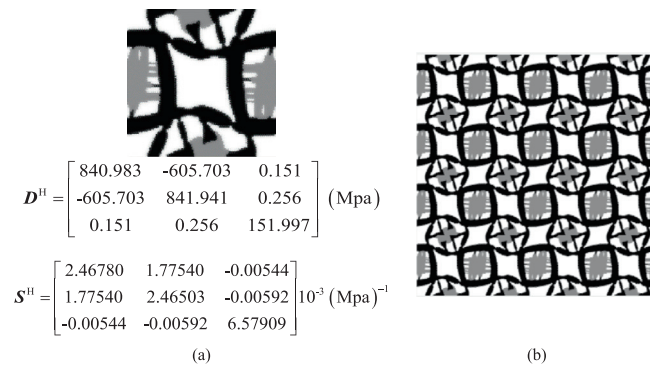
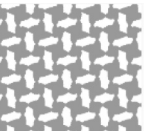
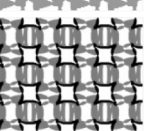
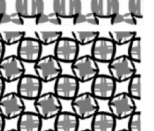
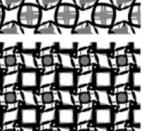


Fig. 9. Optimization solutions of the orthogonal microstructures for the chiral auxetic metamaterials. (a) Bi-material design; (b) 4×4 array of the bi-material unit cell.

Table 4
Optimization results for different volume fractions under orthogonal constraint.

Case	Unit cell	Array (4×4)	D^H (Mpa)	μ_{12}, μ_{21} K^*, G (Mpa)
1			$\begin{bmatrix} 262.569 & -176.737 & -0.027 \\ -176.737 & 262.573 & -0.007 \\ -0.027 & -0.007 & 56.086 \end{bmatrix}$	$-0.671, -0.671$ 42.616, 56.086
2			$\begin{bmatrix} 328.894 & -286.783 & 0.042 \\ -286.783 & 504.304 & -0.079 \\ 0.042 & -0.079 & 64.880 \end{bmatrix}$	$-0.8718, -0.5687$ 64.909, 64.880
3			$\begin{bmatrix} 665.752 & -451.002 & 0.242 \\ -451.002 & 608.880 & -0.285 \\ 0.242 & -0.285 & 97.467 \end{bmatrix}$	$-0.667, -0.733$ 93.158, 97.461
4			$\begin{bmatrix} 858.229 & -631.667 & -0.025 \\ -631.667 & 857.235 & 0.097 \\ -0.025 & 0.097 & 155.799 \end{bmatrix}$	$-0.760, -0.760$ 113.032, 155.799
5			$10^3 \begin{bmatrix} 1.359 & -0.917 & -0.000 \\ -0.917 & 1.359 & 0.000 \\ -0.000 & 0.000 & 0.255 \end{bmatrix}$	$-0.643, -0.643$ 220.875, 254.800

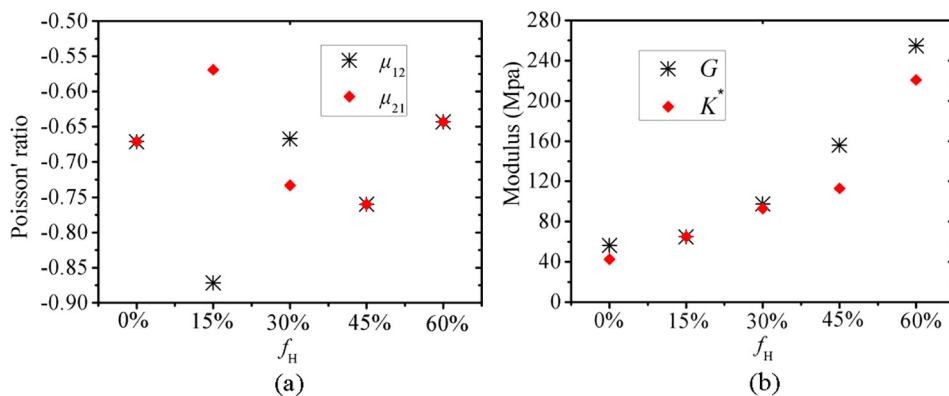


Fig. 10. Properties of the optimized design obtained with different volume fractions of hard materials. (a) Effective Poisson's ratios μ_{12} and μ_{21} ; (b) the quasi-effective bulk modulus K^* and the shear modulus G .

Table 5
Different cases of material volume fraction f_T (total material), f_H (hard material), and f_S (soft material).

f_T	f_H	f_S
30%	12%	18%
40%	16%	24%
50%	20%	30%
60%	24%	36%
70%	28%	42%

asymptotic homogenization (-0.713). This discrepancy may be attributed to the finite-size effects of the finite element model. The details for the displacement and stress are given in [Appendix A](#).

4.5. Finite element simulation of 3D chiral array structures

In this sub-section, we present finite element simulations of 3D periodic array structure composed of the optimized microstructural unit cells. By using the similar method in papers [18,19], we construct the 3D structures from the optimized microstructural unit cells.

Table 6
Optimization results for different total volume fractions under orthogonal constraint.

Case	Unit cell	Array 4 × 4	D^H (Mpa)	μ_{12}, μ_{21} K^*, G (Mpa)
1			$\begin{bmatrix} 225.861 & -137.092 & 0.056 \\ -137.092 & 242.434 & 0.003 \\ 0.056 & 0.003 & 6.731 \end{bmatrix}$	$-0.603, -0.567$ $48.527, 6.731$
2			$\begin{bmatrix} 331.011 & -196.234 & 0.098 \\ -196.234 & 323.735 & -0.076 \\ 0.098 & -0.076 & 26.084 \end{bmatrix}$	$-0.604, -0.617$ $65.5694, 26.084$
3			$\begin{bmatrix} 373.692 & -310.509 & 0.1890 \\ -310.509 & 506.391 & 0.017 \\ 0.190 & 0.0172 & 35.240 \end{bmatrix}$	$-0.825, -0.600$ $67.434, 35.2406$
4			$\begin{bmatrix} 478.993 & -348.951 & 0.360 \\ -348.951 & 555.467 & -0.068 \\ 0.360 & -0.068 & 93.713 \end{bmatrix}$	$-0.727, -0.632$ $84.13, 93.713$
5			$\begin{bmatrix} 649.271 & -419.991 & -0.067 \\ -419.991 & 645.539 & 0.134 \\ -0.067 & 0.134 & 80.388 \end{bmatrix}$	$-0.630, -0.630$ $113.707, 80.388$

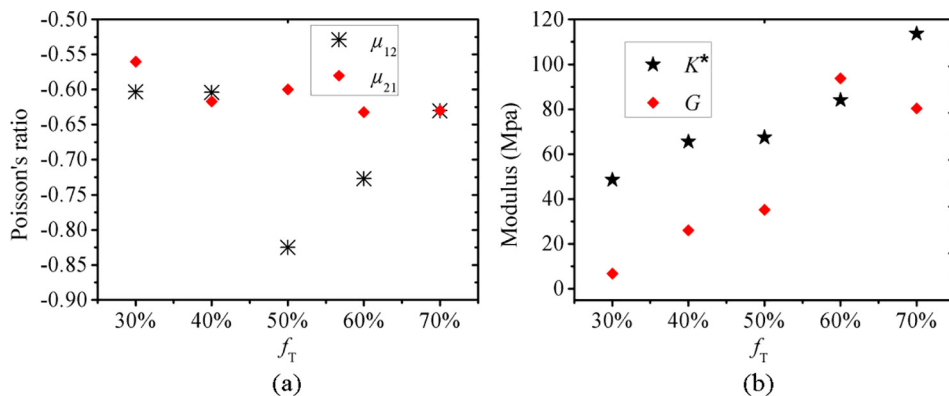


Fig. 11. Properties of the optimized designs with different total material volume. (a) Effective Poisson's ratios μ_{12} and μ_{21} ; (b) quasi-effective bulk modulus K^* and the shear modulus G .

Table 7

Optimization results under orthogonal and isotropic constraints.

Orthogonal microstructure	Isotropic microstructure
$\begin{bmatrix} 579.188 & -343.058 & 0.105 \\ -343.058 & 531.083 & -0.026 \\ 0.105 & -0.026 & 107.908 \end{bmatrix}$ (Mpa)	$\begin{bmatrix} 307.639 & -219.444 & -0.051 \\ -219.444 & 305.795 & 0.050 \\ -0.051 & 0.050 & 263.074 \end{bmatrix}$ (Mpa)
$\mu_{12} = -0.600$	$\mu = -0.713$
$\mu_{21} = -0.643$	$K = 44.125$ Mpa
$K^* = 106.039$ Mpa	$G = 263.074$ Mpa
$G = 107.908$ Mpa	

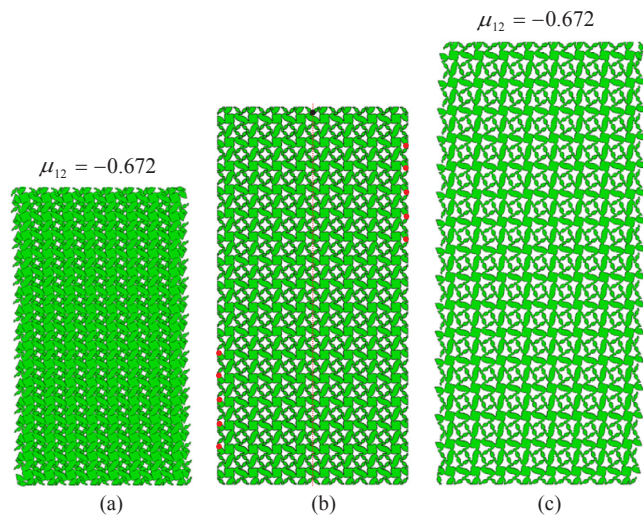


Fig. 13. Finite element simulation results for 8×16 periodic array. (a) Deformation under the y direction compression displacement, 60 mm; (b) undeformed structures assembled by 128 unit cells; (c) deformation under y direction tension displacement, 60 mm.

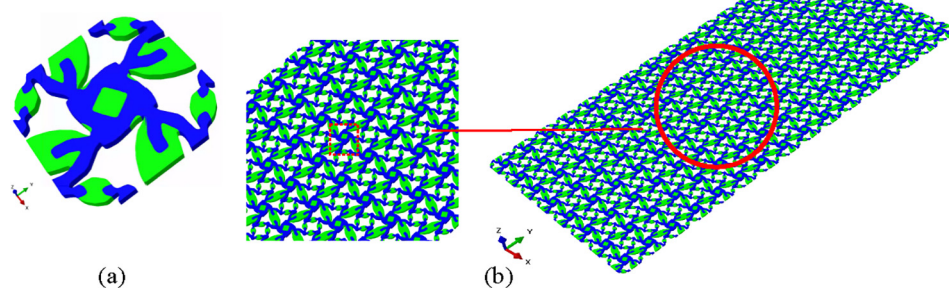


Fig. 12. Geometric models for the isotropy bi-material chiral auxetic metamaterials. (a) unit cell; (b) 8×16 periodic array.

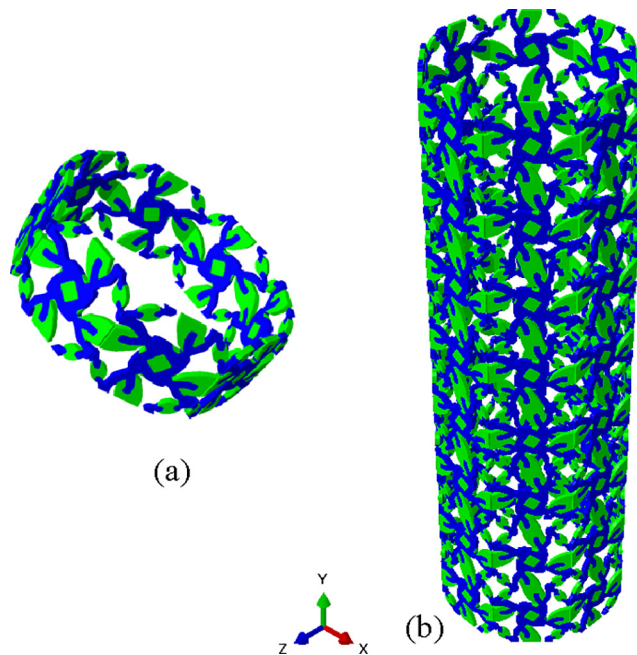
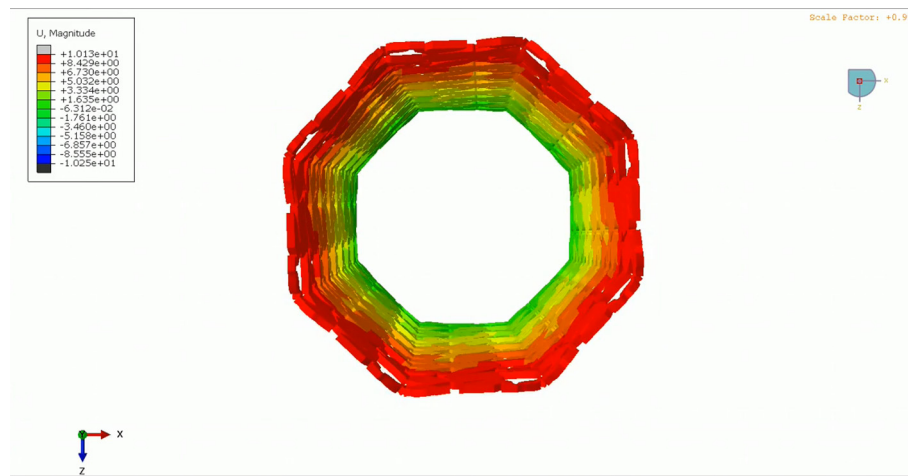


Fig. 14. Three-dimensional chiral rotational tube composed of the optimized bi-material unit cells. (a) Bi-material unit cell; (b) chiral tube.

4.5.1. Chiral auxetic rotational tube

We first consider an auxetic rotational tube constructed from the optimized isotropic microstructure (see Section 4.3), as shown in Fig. 14(b). Each unit cell is first rotated by $45^\circ \times k$ ($k = 1, 2, \dots, 7$), and then connected together to form a circular configuration as shown in Fig. 14(a). The final structure has eight periodic layers in y direction. We expect that this cylinder shell-like structure possesses not only the NPR effect, but also undergoes rotation under an axial loading condition.

The finite element model consists of 6017,020 quadratic tetrahedron solid elements and 9193,537 nodes. We apply a compressing of 10 mm (corresponding to an axial strain of 6.79%) to the upper surface while fixing the bottom surface. As seen from Fig. 15, the structure exhibits a shrinking in the middle cross section and a rotation around y axis, which confirms that this 3D periodic structure has both NPR effect and rotational characteristic. For the details of the deformation process, the readers are referred to the movies (M1, M2) provided in supplement materials.



Movie 1.



Movie 2.

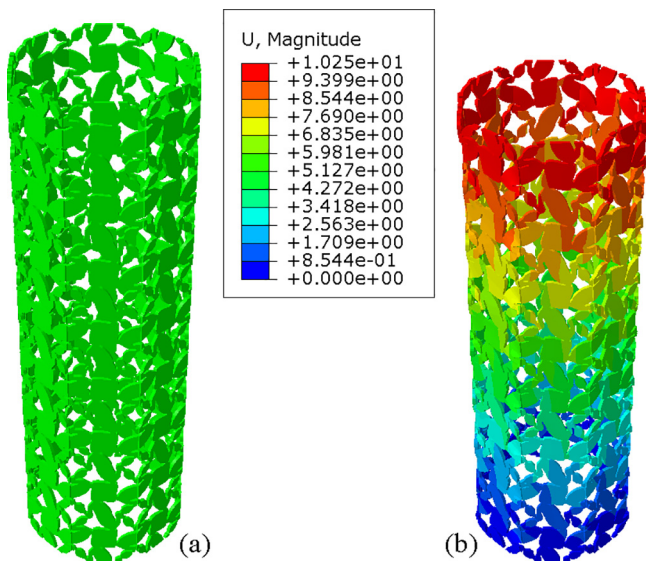


Fig. 15. Finite element simulation of the chiral tube structure. (a) Undeformed shape; (b) displacements under axial load.

4.5.2. Chiral twisting structure

First, a 3D unit cell is assembled with the optimized microstructure (Fig. 16(a)), and then five of such unit cells are assembled together to form a chiral twisting structure, as depicted in Fig. 16(b). We will show through finite element analysis that this chiral structure is able to transform a uniaxial load into a twisting deformation, similarly as the mechanical metamaterial reported in a recent study [18].

The finite element model of the assembled chiral twisting structure consists of 2,336,517 quadratic tetrahedron solid elements and 3,570,124 nodes. All the degrees of freedom at the bottom surfaces are fixed and a displacement of 10 mm (corresponding to an axial strain of 10.87%) along y direction is applied to the upper surface. As can be seen from Fig. 17, this structure exhibits obvious twisting under the uniaxial compression, with a twisting angle $\phi = 16.812^\circ$ at the top surface. The readers are referred to the (M3–M5) provided in supplement materials for details of the deformation process.

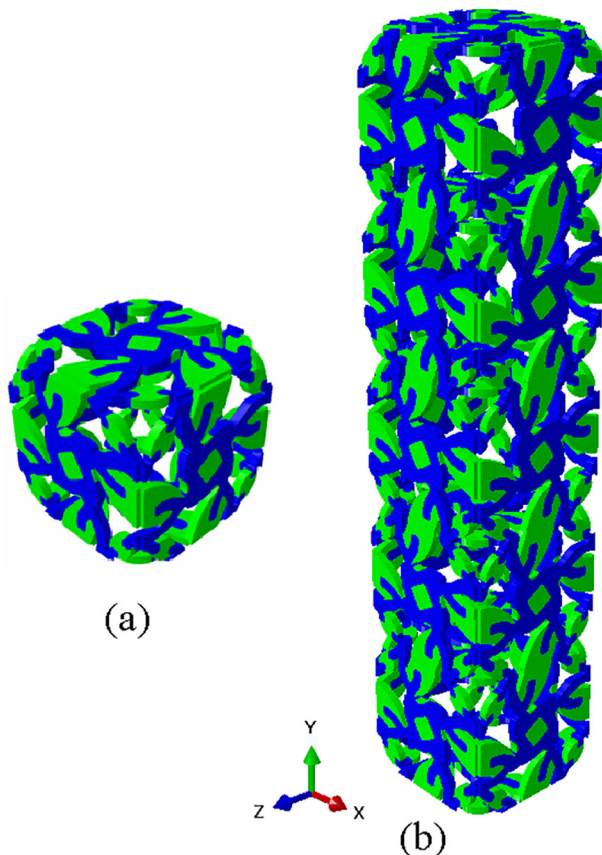
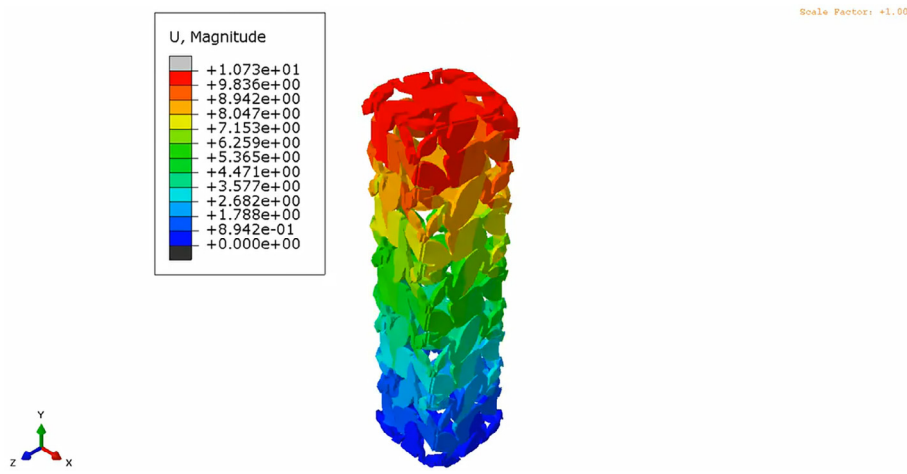
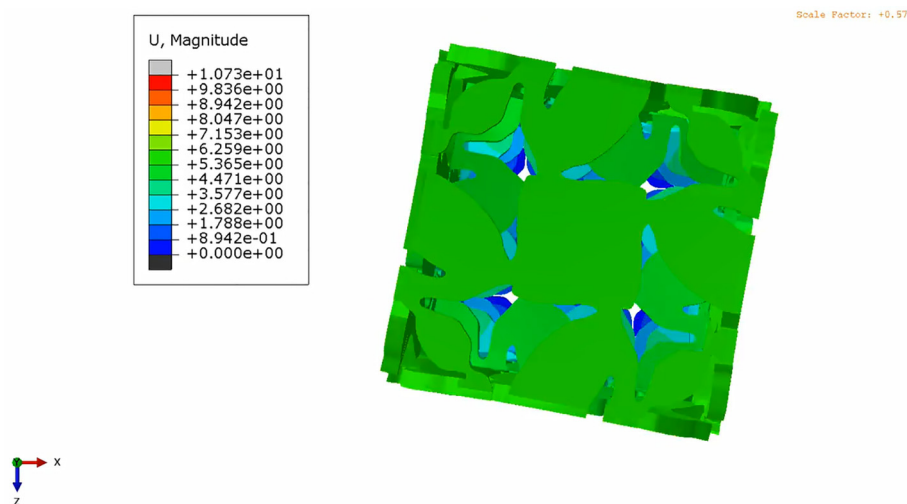


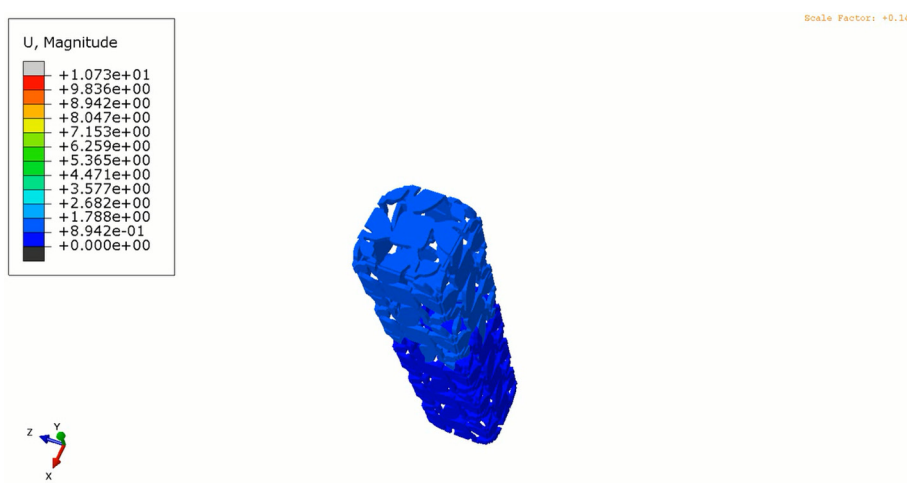
Fig. 16. Mechanical metamaterial twist structures. (a) Unit cell of the three chiral microstructures; (b) bi-material chiral auxetic twisting structure;



Movie 3.



Movie 4.



Movie 5.

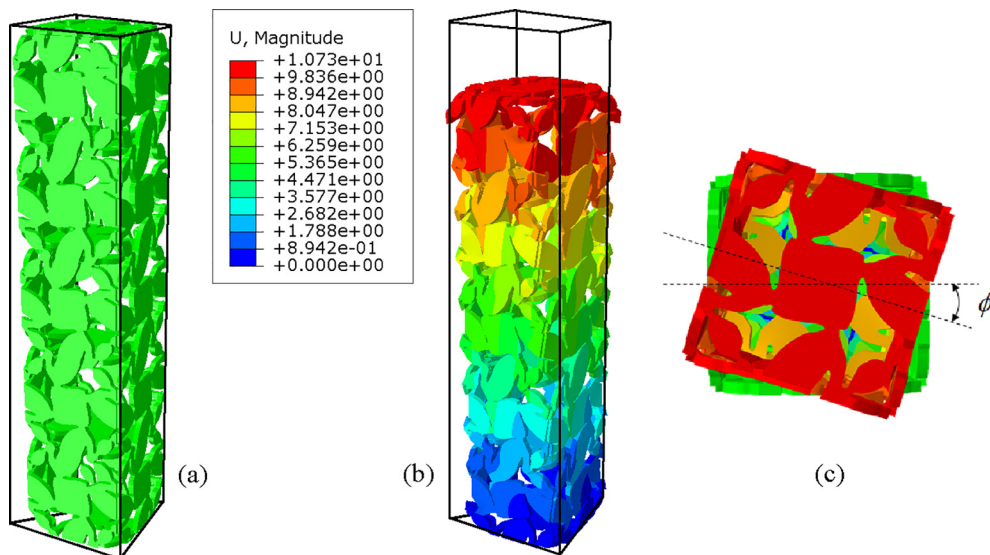


Fig. 17. Finite element simulation of chiral twisting structure. (a) Undeformed shape; (b) displacements under axial load; (c) twisting of top surface.

5. Conclusions

In this paper, we studied topology optimization of bi-material microstructures of metamaterials to achieve chiral auxetic properties. The iPDI model was combined with the bi-material interpolation scheme to represent the material distribution in the unit cells. Well-defined microstructural topologies and material boundaries could be obtained with the proposed optimization model. The optimized negative Poisson's ratio and stiffness of the metamaterials have a dependency on the volume fractions of each material phases. We also found that the stiffness of bi-material chiral auxetic microstructures could be tailored along with the negative Poisson's ratio effect by imposing the orthogonal or isotropic constraints in the present optimization model.

We performed the finite element analysis to verify the Poisson's ratios effects. It was shown that a 3D chiral structure composed of

periodically arrayed optimized unit cells could transform linear uniaxial displacements into twisting deformations.

The optimization results can be used as guidance to the design of artificial multiple-material microstructures for auxetic metamaterials. The method may be also extended to the design of other novel chiral microstructures to achieve specified functional requirements.

Acknowledgements

Financial support of the National Science Fund for Distinguished Young Scholars (Grant No. 11425207) and the Key Program of National Science Foundation of China (Grant No. U1508209) is gratefully acknowledged. Special thank goes to Dr. Yiqiang Wang for the helpful discussions. We are also grateful to professor Krister Svanberg for proving the optimization package MMA.

Appendix A

(see Fig. A).

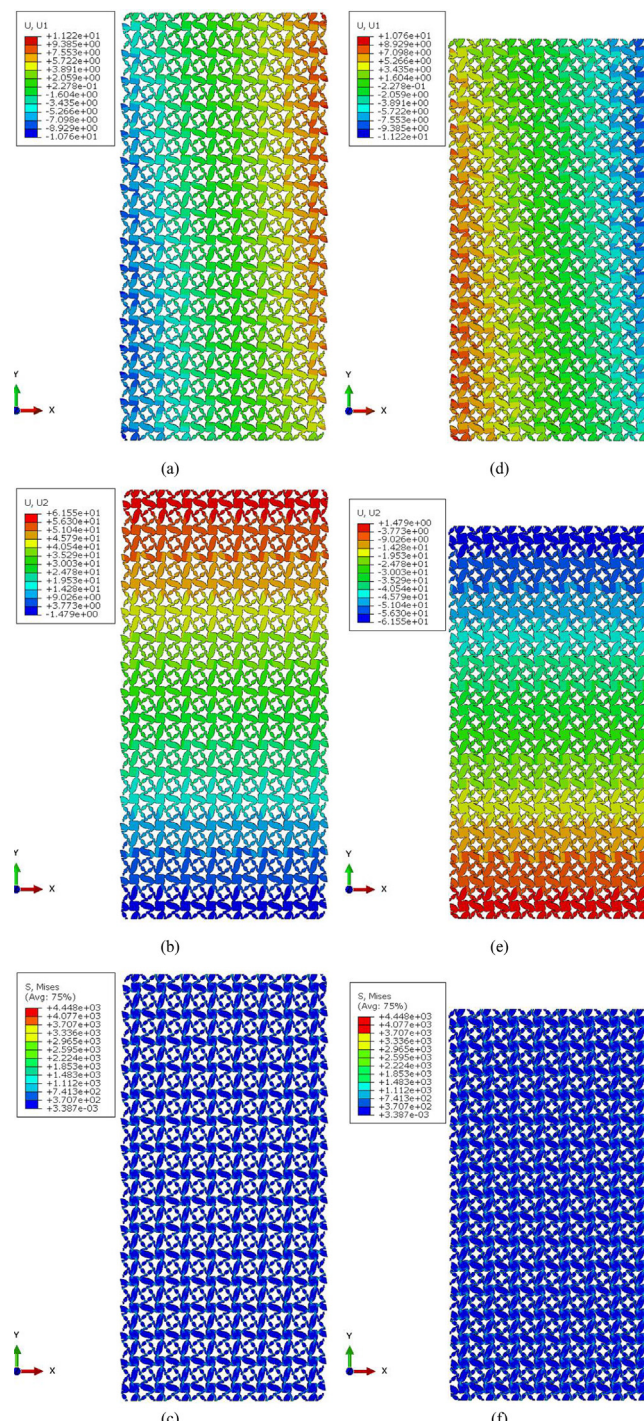


Fig. A. Finite element simulations for tensile (a)-(c) and compressive (d)-(f) conditions of 8×16 array. (a), (d) displacements in x direction; (b), (e) displacements in y direction; (c), (f) von-Mises stress.

References

- [1] Lakes R. Foam structures with a negative Poisson's ratio. *Science* 1987;235:1038–41.
- [2] Saxena KK, Das R, Calius EP. Three decades of auxetics research – materials with negative Poisson's ratio: a review. *Adv Eng Mater* 2016;18:1847–70.
- [3] Kolken HMA, Zadpoor AA. Auxetic mechanical metamaterials. *RSC. Advances* 2017;7:5111–29.
- [4] Ali MN, Busfield JJ, Rehman IU. Auxetic oesophageal stents: structure and mechanical properties. *J Mater Sci Mater Med* 2014;25:527–53.
- [5] Sanami M, Ravirala N, Alderson K, Alderson A. Auxetic materials for sports applications. *Eng Sport* 2014;10(72):453–8.
- [6] Donoghue JP, Alderson KL, Evans KE. The fracture toughness of composite laminates with a negative Poisson's ratio. *Physica Status Solidi B-Basic Solid State Phys* 2009;246:2011–7.
- [7] Choi JB, Lakes RS. Fracture toughness of re-entrant foam materials with a negative Poisson's ratio: experiment and analysis. *Int J Fract* 1996;80:73–83.
- [8] Liu WY, Wang NL, Luo T, Lin ZQ. In-plane dynamic crushing of re-entrant auxetic cellular structure. *Mater Des* 2016;100:84–91.
- [9] Reda H, Elnady K, Ganghoffer JF, Lakiss H. Control of acoustic properties of network materials by finite pre-deformations: applications to 3D auxetic network materials. *Int J Non Linear Mech* 2017;99:1–12.
- [10] Francesco D, Victor AE, Alexey P. Advances in mechanics of microstructured media and structures. Springer; 2018.
- [11] Karathanasopoulos N, Reda H, Ganghoffer JF. Designing two-dimensional

- metamaterials of controlled static and dynamic properties. *Comput Mater Sci* 2017;138:323–32.
- [12] Hou Y, Tai YH, Lira C, Scarpa F, Yates JR, Gu B. The bending and failure of sandwich structures with auxetic gradient cellular cores. *Compos Part A-Appl Sci Manuf* 2013;49:119–31.
- [13] Ju JY, Summers JD. Compliant hexagonal periodic lattice structures having both high shear strength and high shear strain. *Mater Des* 2011;32:512–24.
- [14] Prall D, Lakes RS. Properties of a chiral honeycomb with a Poisson's ratio of -1. *Int J Mech Sci* 1997;39:305–14.
- [15] Wang K, Chang YH, Chen YW, Zhang C, Wang B. Designable dual-material auxetic metamaterials using three-dimensional printing. *Mater Des* 2015;67:159–64.
- [16] Lu ZX, Wang QS, Li X, Yang ZY. Elastic properties of two novel auxetic 3D cellular structures. *Int J Solids Struct* 2017;124:46–56.
- [17] Fu MH, Zheng BB, Li WH. A novel chiral three-dimensional material with negative Poisson's ratio and the equivalent elastic parameters. *Compos Struct* 2017;176:442–8.
- [18] Frenzel T, Kadic M, Wegener M. Three-dimensional mechanical metamaterials with a twist. *Science* 2017;358:1072–4.
- [19] Wang XT, Li XW, Ma L. Interlocking assembled 3D auxetic cellular structures. *Mater Des* 2016;99:467–76.
- [20] Thiel M, Rill MS, von Freymann G, Wegener M. Three-dimensional bi-chiral photonic crystals. *Adv Mater* 2009;21(46):4680–2.
- [21] Soukoulis CM, Martin W. Past Achievements and future challenges in 3D Photonic metamaterials. *Nat Photonics* 2011;5:523–30.
- [22] Ha CS, Hestekin E, Li JH, Plesha ME, Lakes RS. Controllable thermal expansion of large magnitude in chiral negative Poisson's ratio lattices. *Physica Status Solidi B-Basic Solid State Phys* 2015;252:1431–4.
- [23] Wang MY, Wang XM, Guo DM. A level set method for structural topology optimization. *Comput Methods Appl Mech Eng* 2003;192:227–46.
- [24] Bendsoe MP, Sigmund O. Topology optimization by distribution of isotropic material. Springer; 2004. [pp. 1–69].
- [25] Aage N, Andreassen E, Lazarov BS, Sigmund O. Giga-voxel computational morphogenesis for structural design. *Nature* 2017;550(7674):84.
- [26] Zhu JH, Zhang WH, Xia L. Topology optimization in aircraft and aerospace structures design. *Arch Comput Methods Eng* 2016;23:595–622.
- [27] Wang XJ, Xu SQ, Zhou SW, Xu W, Leary M, Choong P, et al. Topological design and additive manufacturing of porous metals for bone scaffolds and orthopaedic implants: a review. *Biomaterials* 2016;83:127–41.
- [28] Wang YQ, Luo Z, Zhang N, Kang Z. Topological shape optimization of microstructural metamaterials using a level set method. *Comput Mater Sci* 2014;87:178–86.
- [29] Sigmund O. Materials with prescribed constitutive parameters – an inverse homogenization problem. *Int J Solids Struct* 1994;31:2313–29.
- [30] Huang XD, Xie YM. Evolutionary topology optimization of continuum structures: methods and applications. John Wiley & Sons; 2010.
- [31] Schwerdtfeger J, Wein F, Leugering G, Singer RF, Körner C, Stingl M, et al. Design of auxetic structures via mathematical optimization. *Adv Mater* 2011;23:2650–4.
- [32] Andreassen E, Lazarov BS, Sigmund O. Design of manufacturable 3D extremal elastic microstructure. *Mech Mater* 2014;69:1–10.
- [33] Xia L, Breitkopf P. Design of materials using topology optimization and energy-based homogenization approach in Matlab. *Struct Multidiscip Optim* 2015;52:1229–41.
- [34] Clausen A, Wang FW, Jensen JS, Sigmund O, Lewis JA. Topology optimized architectures with programmable Poisson's ratio over large deformations. *Adv Mater* 2015;27:5523–7.
- [35] Ganghoffer JF, Goda I, Novotny AA, Rahouadj R, Sokolowski J. Homogenized couple stress model of optimal auxetic microstructures computed by topology optimization. *ZAMM-J Appl Math Mech/Zeitschrift für Angewandte Mathematik und Mechanik* 2017;1–22.
- [36] Vogiatzis P, Chen SK, Wang X, Li TT, Wang LF. Topology optimization of multi-material negative Poisson's ratio metamaterials using a reconciled level set method. *Comput Aided Des* 2017;83:15–32.
- [37] Wang Y, Gao J, Luo Z, Brown T, Zhang N. Level-set topology optimization for multimaterial and multifunctional mechanical metamaterials. *Eng Optim* 2016;49:22–42.
- [38] Haghpanah B, Papadopoulos J, Mousanezhad D, Nayeb-Hashemi H, Vaziri A. Buckling of regular, chiral and hierarchical honeycombs under a general macroscopic stress state. *Proc R Soc A-Math Phys Eng Sci* 2014;470:20130856.
- [39] Bornengo D, Scarpa F, Remillat C. Evaluation of hexagonal chiral structure for morphing airfoil concept. *Proc Inst Mech Eng Part G-J Aerospace Eng* 2005;219:185–92.
- [40] Kang Z, Wang YQ. A nodal variable method of structural topology optimization based on Shepard interpolant. *Int J Numer Meth Eng* 2012;90:329–42.
- [41] Wang YQ, Kang Z, He QZ. Adaptive topology optimization with independent error control for separated displacement and density fields. *Comput Struct* 2014;135:50–61.
- [42] Kang Z, Wang YQ. Structural topology optimization based on non-local Shepard interpolation of density field. *Comput Methods Appl Mech Eng* 2011;200:3515–25.
- [43] Xia Q, Shi T. Optimization of composite structures with continuous spatial variation of fiber angle through Shepard interpolation. *Compos Struct* 2017;182:273–82.
- [44] Xia Q, Shi T. A cascadic multilevel optimization algorithm for the design of composite structures with curvilinear fiber based on Shepard interpolation. *Compos Struct* 2018;188:209–19.
- [45] Bendsoe MP, Sigmund O. Material interpolation schemes in topology optimization. *Arch Appl Mech* 1999;69:635–54.
- [46] Torquato S, Sigmund O. Design of materials with extreme thermal expansion using a three-phase topology optimization method. *J Mech Phys Solids* 1997;45:1037–67.
- [47] Huang X, Radman A, Xie YM. Topological design of microstructures of cellular materials for maximum bulk or shear modulus. *Comput Mater Sci* 2011;50(6):1861–70.
- [48] Svaberg K. The method of moving asymptotes - a new method for structural optimization. *Int J Numer Methods Eng* 1987;24:359–3573.
- [49] Vasiliev Valery, Morozov Evgeny. Mechanics and analysis of composite materials. Elsevier; 2001.
- [50] Carta G, Brun M, Baldi A. Design of a porous material with isotropic negative Poisson's ratio. *Mech Mater* 2016;97:67–75.
- [51] Shan S, Kang SH, Zhao Z, Fang L, Bertoldi K. Design of planar isotropic negative Poisson's ratio structures. *Extreme Mech Lett* 2015;4:96–102.